Collision cross sections of N_2 by H^+ impact at keV energies within time-dependent density-functional theory

W. Yu,[1,2] C.-Z. Gao,[3,*] Y. Zhang,[1,2] F. S. Zhang,[4] R. Hutton,[1,2] Y. Zou,[1,2] and B. Wei[1,2,†]

[1]*Institute of Modern Physics, Department of Nuclear Science and Technology, Fudan University, Shanghai 200433, China*

[2]*Key Laboratory of Nuclear Physics and Ion-beam Application (MOE), Fudan University, Shanghai 200433, China*

[3]*Institute of Applied Physics and Computational Mathematics, Beijing 100088, China*

[4]*College of Nuclear Science and Technology, Beijing Normal University, Beijing 100875, China*

(Received 22 December 2017; published 23 March 2018)

We calculate electron capture and ionization cross sections of N_2 impacted by the H^+ projectile at keV energies. To this end, we employ the time-dependent density-functional theory coupled nonadiabatically to molecular dynamics. To avoid the explicit treatment of the complex density matrix in the calculation of cross sections, we propose an approximate method based on the assumption of constant ionization rate over the period of the projectile passing the absorbing boundary. Our results agree reasonably well with experimental data and semi-empirical results within the measurement uncertainties in the considered energy range. The discrepancies are mainly attributed to the inadequate description of exchange-correlation functional and the crude approximation for constant ionization rate. Although the present approach does not predict the experiments quantitatively for collision energies below 10 keV, it is still helpful to calculate total cross sections of ion-molecule collisions within a certain energy range.

DOI: 10.1103/PhysRevA.97.032706

I. INTRODUCTION

In the past decades, the investigation of proton-molecule collisions has received great attention in many fields, such as ultrafast physics, structural chemistry, astrophysics, and radiation therapy [1–3]. One of the fundamental goals is to probe the structural and dynamical properties of the molecules with little knowledge. Out of the observables extensively measured and analyzed in experiments, the cross sections' database are probably the most abundant, typically including types of collision-induced excitation, charge transfer, ionization, and fragmentation, and even more state-to-state cross sections can readily be accessible achieved by novel experimental techniques [3,4]. In this context, the interpretation of experimental data is nontrivial, and presents a challenge to collision theories as well as numerical modelings.

In studying proton-molecule collisions, a number of theoretical models have been developed for a wide variety of experimental data qualitatively and/or (semi)quantitatively in the different energy ranges [5–7], which is mainly determined by the level of theoretical description, i.e., classical, semiclassical, and quantum-mechanical treatments. For example, the classical trajectory Monte Carlo (CTMC) method [8] based on the classical treatment of individual particle trajectories predicts well the experiments at impact energies of more than 10 keV [9], and the classical over-the-barrier (COB) approach [10] using Coulomb-like interaction potentials to represent the collision participants yields qualitative agreements with experiments at energies up to tens of keV [11]. Semiclassical descriptions usually refer to the treatments using the wave functions for electrons and meanwhile classical mechanics for nuclei, such as two-center atomic-orbital close-coupling (TC-AOCC) method [12,13] and the time-dependent density-functional theory (TDDFT) [14,15]. Both methods solve the time-dependent Schrödinger equations (TDSE), but the former operates the approximation by expanding the active electron's total wave function onto bound atomic orbitals centered on the moving ions multiplied by the plane-wave electron translational factor. In contrast, the latter treats the interacting electrons by independent particles subjected to an effective external potential, and the quality of the results depends on the construction of the effective Hamiltonian as well as initial wave functions [16]. The TC-AOCC model is typically applicable in the energy range of 50 eV–10 keV, while the TDDFT approach can be extended much broader in the energy spectrum. A fully quantum-mechanical approach is the well-established quantum-mechanical molecular-orbital close-coupling (QMOCC) method [17,18], which requires accurate potential energy curves or surfaces and associated coupling matrix elements as inputs, and for the energies of 10^{-5} eV-10 keV QMOCC results are believed to be reliable and robust. In this work, we shall theoretically investigate molecular collisions at energies of 0.6–3000 keV. Within the consideration of the applicable energy region of the above approaches and the balance between the computational accuracy and costs, the TDDFT coupled nonadiabatically to molecular dynamics [14,19] is used throughout the work.

In the applications of the TDDFT-MD model to molecular collisions, observables such as electron capture and ionization probabilities can, in principle, be extracted from the single-electron Kohn-Sham orbitals (KSOs) [20,21]. Specifically for the electron capture process, the probabilities are closely

*Corresponding author: czgao88@hotmail.com

†Corresponding author: brwei@fudan.edu.cn

associated with the final scattering states of the projectile. In general, within the TDDFT-based framework an accurate description on the final states depends on several aspects, such as the interaction potential, the representation and propagation of molecular orbitals, and so on. Lüdde *et al.* [22] first devised a general scheme to calculate total capture probabilities for a many-electron scattering process, through evaluating half-space one-particle overlaps. Their proposition avoids treating explicitly all the channels contributing to the total probabilities and has inspired several theoretical modelings subsequently. Kirchner and his coworkers studied a variety of ion-molecule collisions (H^+-H_2O [23,24], H^+-CH_4 [25], He^+-H_2O [26], O^{6+}-(H_2O, CH_4) [27]) at high collision energies using the non-perturbative two-center basis generator method (TC-BGM). In their implementation, the spectral representation of the molecular Hamiltonian and the basis expansion of the molecular wave function are very crucial. The (state-resolved) transition probabilities for electronic processes is thus evaluated directly from determinants of the one-particle density matrix, and can quantitatively predict the experimental data in a wide range of energies. Wang *et al.* [28] implemented coordinate space translation (CST) into the TDDFT scheme to study H^+-H_2O collisions [29]. The CST method involves a translation technique after collision that is to reset all nucleus coordinates and KSOs in the simulation box, moving the projectile to the origin of the box and meanwhile allowing the target to be scattered away. It should be noted that the aforementioned approaches extract the transition probabilities quantum-mechanically from the determinants' overlap integrals, giving results consistent with experiments in the energy range of interest provided the final scattering states have been properly described. In the present study, we present an approximate method to calculate electron capture and ionization probabilities from KSOs without explicitly accounting for overlap integrals. Our results can compare reasonably well to available experiments in the considered energy range.

In this study, we investigate H^+-N_2 collisions at keV energies in the framework of TDDFT-MD model. We calculate the electron capture and ionization cross sections, for which abundant experimental data are ready to be compared in a wide energy range. In the calculations, six collision configurations are employed to account for orientation effects. This article is outlined as follows. Section II briefly introduces the basics of the TDDFT-MD model, the strategy to extract associated cross sections, and numerical details for the calculations. Followed by the results' discussion in Sec. III, where we mainly discuss the electron capture and ionization cross sections, and comparisons to other data sources are performed where available. The conclusion is finally summarized in Sec. IV.

II. METHODOLOGY

A. Ehrenfest dynamics coupled with TDDFT

In the framework of the TDDFT, all physical quantities of an auxiliary time-dependent system can, in principle, be determined by the knowledge of the time-dependent density, as demonstrated in the seminal work of Runge and Gross in Ref. [14]. In comparison to the time-dependent Schrödinger equations (TDSE) method, TDDFT actually describes an ensemble of noninteracting particles [i.e., Kohn-Sham (KS) systems] moving in an effective external potential, which is connected to the real interacting systems uniquely through the electronic density $\rho(\mathbf{r},t) = \sum_{j=1}^{N_e} \psi_j^*(\mathbf{r},t)\psi_j(\mathbf{r},t)$, where single-particle (s.p.) wave functions $\{\psi_j(\mathbf{r},t)\}$ fulfill the time-dependent KS equations (TDKS) formulated as below (in atomic units)

$$i\frac{\partial}{\partial t}\psi_j(\mathbf{r},t) = \left[-\frac{1}{2}\nabla^2 + V_{\rm ne}(\mathbf{r}) + V_{\rm H}[\rho](\mathbf{r},t) + V_{\rm xc}[\rho](\mathbf{r},t)\right]\psi_j(\mathbf{r},t), \quad j = 1,2,\ldots,N_e\,. \tag{1}$$

For simplicity, the spin notation is omitted here. The total electronic density is constructed by summing the squared occupied KS orbitals (KSOs) up to the total number of valence electrons N_e. The effective potential on the right side of Eq. (1) is composed of electron-nucleus potential ($V_{\rm ne}$), direct electron-electron (or Hartree) potential ($V_{\rm H}$), and the exchange-correlation (xc) potential ($V_{\rm xc}$), where the last two terms are of the form of functionals of electronic density. It is well known that the xc potential incorporates the so-called quantum many-body effects, whose exact expression has not yet been established to date. Thus this needs to be approximated in practical cases. Here we applied the local density approximation (LDA) in its adiabatic form augmented by a self-interaction correction (SIC) [30,31] to deal with time-dependent ion-molecule collisions [32,33], which ensures a correct Coulombic asymptotic behavior of the effective potential for the electron in the system. To construct an exact effective potential, a more accurate treatment such as an optimized potential method (OPM) can be the choice, which has already been favored in ion-atom collisions [34,35]; particularly it can yield more physical results of low-energy doubly differential cross section [34].

In general, ionic dynamics are governed by the force acting on the moving ions, which is therefore closely associated with both the ionic $\{\mathbf{R}_I\}$ and electronic positions $\{\mathbf{r}\}$. In this work, we treat it on the level of classical molecular dynamics (MD), which satisfies the following Newtonian equation of motion according to Ehrenfest theorem [36]:

$$M_I\frac{d^2\mathbf{R}_I(t)}{dt^2} = -\nabla_{\mathbf{R}_I}\left[\int d^3\mathbf{r}\rho(\mathbf{r},t)V_{\rm ne}(\mathbf{r}-\mathbf{R}_I) + \sum_{I\neq J}^{N_{\rm ion}}\frac{Z_I Z_J}{|\mathbf{R}_I(t)-\mathbf{R}_J(t)|}\right], \tag{2}$$

for the Ith ion with the mass M_I and the corresponding charge Z_I, where I is ion index, an integer from 1 to $N_{\rm ion}$ (the total number of ions of the system). It should also be noted that the coupling between ionic ($\mathbf{R}_I$) and electronic [$\rho(\mathbf{r},t)$] degrees of freedom appears in Eq. (2) via the electron-nucleus potential which is usually approximated by the norm-conserving pseudopotentials [37]. Here, we emphasize that the simultaneous propagation of Eqs. (1) and (2) in real time and real space forms the basis of Ehrenfest dynamics within TDDFT (ED-TDDFT).

Although ED-TDDFT has been widely applied in ion-atom and ion-molecule collisions [32,33,38–40] with considerable success, it is still to be noted that the present Ehrenfest approach

is perfectly suitable for the cases [15] where (i) a single path in nuclear dynamics is dominant and (ii) the branching of nuclear trajectories for different reaction processes should be avoided. In other words, Ehrenfest dynamics is essentially a mean-field treatment where the nuclear trajectory evolves on an averaged potential surface, and thus potential and force are evaluated as mean expectation values. Illustrative results for the two-electron collision system (H^++He) [41,42] have shown a good agreement with the experimental data of ionization and capture differential cross sections, where the last of these (capture processes [42]) at small angles revealed the importance of nuclear trajectory effects, and must be treated with care, e.g., based on the semiquantal eikonal approximation, which is, however, beyond the capability of our used model.

B. Extraction of observables

In the current work, electronic dynamics is described only for ten valence electrons since the $1s$ electrons of atomic nitrogen are deeply bound to the nuclei. For the $H^+ + N_2$ collision under consideration, we find that the target electron loss is primarily channeled into two paths, namely, electrons captured by the scattered proton and that of direct electron emissions, thus resulting in the N_2 target being ionized to its allowed charge states. The entire collision processes can simply be described as

$$H^+ + N_2 \rightarrow H^{p+} + N_2^{q+} + me^- \,, \tag{3}$$

with $p + q\text{-}m = 1$ due to charge conservation, where m signifies continuum-state electrons. Here we concentrate on estimating the electron capture and ionization probabilities involved in this study. To this end, we begin with the loss probability based on the well-established strategy proposed by Ullrich [43], which is originally derived from an exact definition of multiple ionization probabilities through the full many-body wave functions and has been successfully applied to tackle the nonequilibrium ionization dynamics in molecules exposed to strong laser fields. In what follows, we first revisit the essential results presented in Ref. [43].

Suppose the full space can be divided into two regions: the simulation box V and its complement $\overline{V}$, the many-body wave functions are thus separated into bound- and continuum-state parts, respectively. The electronic density found in the volume of $\overline{V}$ (outside the numerical box V) corresponds to continuum contributions. The orbital-resolved bound and/or continuum probability at the evolving time t can be defined as

$$p_j(t) = \int_V d^3r |\psi_j(\mathbf{r},t)|^2 \,, \tag{4}$$

$$\overline{p}_j(t) = \int_{\overline{V}} d^3r |\psi_j(\mathbf{r},t)|^2 \,. \tag{5}$$

On this basis, the electron loss probability $P_k^{\rm loss}$ for the charge state k can be approximated by multinomial statistics [43]. As a result, it is quite straightforward to compute the total electron loss probability $P_{\rm tot}^{\rm loss}$ by summing over all the possible contributions

$$P_{\rm tot}^{\rm loss}(t) = \sum_{k=0}^{N_e} k P_k^{\rm loss}(t) = \sum_{j=1}^{N_e} \overline{p}_j(t) \,, \tag{6}$$

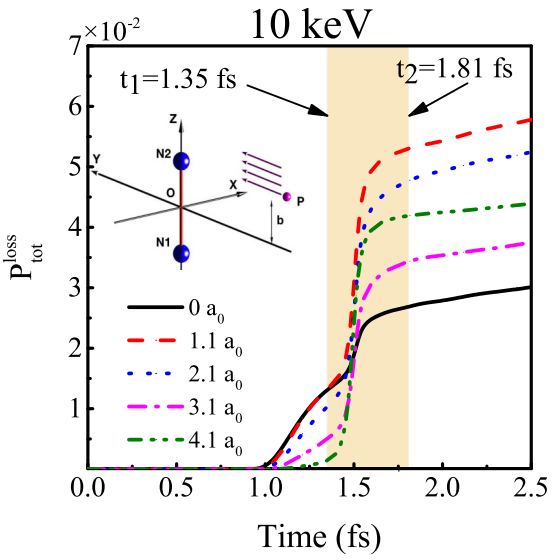

FIG. 1. Total electron loss probabilities as a function of time at 10 keV. Results for typical impact parameters $b = 0$, 1.1, 2.1, 3.1, and 4.1 a_0, are shown. The shadow area represents the time interval for the projectile traversing the absorbing boundary, and t_1 and t_2 denote the starting and ending time instants, respectively. For completeness, the collision configuration is also presented in the inset, see the text for more details.

where $\overline{p}_j(t)$ indicates the electron loss probability for the jth KS orbital. According to Eq. (6), an illustration of total electron loss probabilities at an impact energy of 10 keV is presented in Fig. 1 for several typical impact parameters for the selected collision configuration as indicated in the inset. Depending on the slope of the electron loss curve, two main mechanisms accounting for the electron loss can be clearly identified, that is direct electron emission and electron capture, where the last is visualized by an abrupt increasing in the electrons yield after the time t_1 at which the scattered proton is approaching the absorbing layers placed at the edge of the simulation box.

To understand the physics in Fig. 1, there are two points to be emphasized. (i) Direct electron emission exists in the entire collision process, but the emission rate may not be constant and should depend on the impact energy and also the propagation time. (ii) Electrons captured by the moving proton have some probabilities to be detached, which is also dependent on the impact energy [44,45]. In this work, we did not treat explicitly the detached electrons and instead we consider those contributions to the total ionization. In experiments, these two electronic processes are usually quantified through the ionization and capture probabilities and associated cross sections. For the electron capture probabilities, from a quantum-mechanical viewpoint, it requires the information of final asymptotic scattering states, which has become the standard solution in the theoretical studies of ion-atom and ion-molecule collisions, see Refs. [23,24,29,35,46]. Different from previous final-state analysis, we here propose an indirect approach presented in the following to approximately extract the electron capture probabilities from the continuum probabilities $\bar{p}_j(t)$. The resultant cross sections show good agreements

with experimental results in a large wide range of high-impact energies.

In our calculations, electron loss is numerically recorded by using the absorbing boundary conditions with finite width at the interface of V and $\overline{V}$, which cannot only absorb direct ionized electrons, but also count in those captured by the proton when it passes over the prescribed boundary, see Fig. 1. It is reasonable to assume that the electron capture occurs effectively in a small volume Υ in the vicinity of the projectile, and for the proton the effective radius is typically of the order of magnitude of several a_0, e.g., for H^+ impinging on the Be atoms [47] and LiF surface [48] at keV energies, the used radii for electron capture are 6 and 4 a_0, respectively, which clearly indicates that the volume radius has to be chosen with care for specific ion-target collisions, as an oversized volume will certainly contain fractions of the bound electrons of the target, and a smaller one will underestimate the capture cross sections. By performing a series of test calculations, we find that 6 a_0 is a good choice to ensure a good convergence of the cross sections, which will be discussed in more details in Sec. III A.

Our procedure to extract the electron capture probabilities needs to define two time instants, t_1 and t_2, at which the volume Υ just begins to enter into and leave out the absorbing layers, respectively, which are indicated in Fig. 1. We assume that the straight-line approximation is fulfilled in this work, so that t_1 and t_2 are impact-parameter-independent for the given impact energy. A second assumption is that the electron ionization rate $W_j^{\rm EI}$ does not change significantly over the time interval (t_2-t_1) at the attosecond time scale, see the shadow area in Fig. 1. Accordingly, we roughly estimate the ionization rate over (t_2-t_1) using the midpoint formula

$$W_j^{\rm EI} = \frac{\frac{d}{dt}\overline{p}_j(t)\big|_{t_1-\Delta t} + \frac{d}{dt}\overline{p}_j(t)\big|_{t_2+\Delta t}}{2}, \quad \Delta t \geqslant 0\,, \tag{7}$$

where Δt is introduced as a smoothing factor, i.e., $\Delta t = \alpha(t_2 - t_1) = \alpha t_{2-1}$, where α is a positive empirical parameter that is typically smaller than 0.6. The selection of α together with the radius of Υ will be detailed in the following, see Sec. III A. Within this approximation, the electron capture probability for the j orbital is then calculated approximately by subtracting orbital-specified loss probability from $\overline{p}_j(t)$,

$$p_j^{\rm cap} = \overline{p}_j(t_2) - \overline{p}_j(t_1) - (t_2 - t_1)W_j^{\rm EI}\,, \tag{8}$$

note that the calculated $p_j^{\rm cap}$ describes the electron capture probability at t_2, which is merely an approximation to the stationary capture probability at the final scattering time. It is noted that after collision ($t > t_2$) the electron loss probability is slightly going up when the time elapses, which may indicate that collision-induced resonance states or autoionization states probably occur [49]. This phenomena will certainly influence the ionization processes at large times ($t \to \infty$), but not the capture processes since the captured electrons are evaluated over the time interval (t_2-t_1) by the absorbing boundary. Therefore, the total electron capture probability is calculated by considering all KSOs' contributions as

$$P_{\rm tot}^{\rm cap} = \sum_{j=1}^{N_e} p_j^{\rm cap}. \tag{9}$$

For the impact energy $E_{\rm kin}$, the orbital-resolved electron loss and capture cross sections are obtained by integrating over the impact parameter b as

$$\sigma_j^{\rm loss}(E_{\rm kin}) = 2\pi \int \overline{p}_j(b) b db\,, \tag{10}$$

$$\sigma_j^{\rm cap}(E_{\rm kin}) = 2\pi \int p_j^{\rm cap}(b) b db\,. \tag{11}$$

The corresponding total cross sections are simply calculated by taking into account the contributions from all s.p. orbitals

$$\sigma_{\rm tot}^{\rm loss}(E_{\rm kin}) = \sum_{j=1}^{N_e} \sigma_j^{\rm loss}(E_{\rm kin})\,, \tag{12}$$

$$\sigma_{\rm tot}^{\rm cap}(E_{\rm kin}) = \sum_{j=1}^{N_e} \sigma_j^{\rm cap}(E_{\rm kin})\,. \tag{13}$$

As a consequence, the ionization cross section is calculated by an indirect approach, namely the difference between the total electron loss and capture cross section

$$\sigma_j^{\rm ion}(E_{\rm kin}) = \sigma_j^{\rm loss}(E_{\rm kin}) - \sigma_j^{\rm cap}(E_{\rm kin})\,, \tag{14}$$

$$\sigma_{\rm tot}^{\rm ion}(E_{\rm kin}) = \sum_{j=1}^{N_e} \sigma_j^{\rm ion}(E_{\rm kin})\,. \tag{15}$$

C. Numerical details

In the present study, all calculations were performed on a three-dimensional coordinate-space grid representation [19]. In practice, we employ a cubic simulation box of 72^3 grid points with equal grid spacing in the three directions $\Delta x(y,z) = 0.59$ a_0, amounting to 373248 grid points on which the wave functions, density, and potentials are numerically discretized. The ground state of the N_2 molecule was computed by solving the stationary KS equations [50] using the damped gradient method [51], resulting in the calculated equilibrium bond separation of 2.05 a_0 and the ionization potential ($E_{\rm IP}$) of 15.8 eV, in good agreement with experimental results 2.08 a_0 [52] and 15.6 eV [53], respectively. To proceed with the collision process, six typical different initial configurations [54] were employed by orienting the molecular axis along the three axes and the bisectors of XY, XZ, and YZ planes, schematically displayed in Figs. 2(a) to 2(f). The time propagation is achieved by utilizing the time-splitting technique [55] to solve Eq. (1) and by using the Verlet algorithm [56] to integrate Eq. (2). The time step is set to 0.0003 fs, sufficiently small to maintain the numerical stability. We use the absorbing boundary conditions (ABS) implemented at the edge of the numerical box to evaluate the electron loss in the collisions.

The proton is initially placed at the position (0, −20 a_0, b), while the center of mass of molecular N_2 is set to the origin at rest in the beginning. The magnitude of the initial proton velocity is determined by the given kinetic energy with the relation $\sqrt{2E_{\rm kin}/m_{\rm p}}$ ($m_{\rm p}$ is the mass of proton), and its direction is exclusively pointing towards the positive Y axis. The impact parameter b increases along the positive Z axis, and is mostly varied in the range of $0.0 \leqslant b \leqslant 11.9$ a_0. To reduce the computational time, we roughly divide the b into two regions in

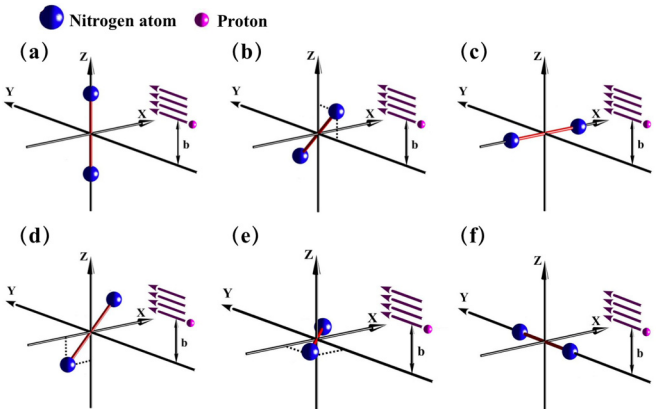

FIG. 2. Schematic of collision configurations of N_2 molecule (large blue balls) scattered by the proton (small pink balls). Six representatives are displayed with the molecular axis aligned (1) along the X, Y, and Z axes, respectively, corresponding to (c), (f), and (a); (2) along the bisector of XY, XZ, and YZ planes, see (e), (d), and (b), respectively. The center of mass of N_2 molecule is initially placed at the origin, while the proton sitting initially at the position (0, -20 a_0, b) with initial velocity $\sqrt{2E_{\rm kin}/m_{\rm p}}$, moves towards the target along the positive Y axis with the impact parameter b increasing along the positive Z axis, as indicated in the inset.

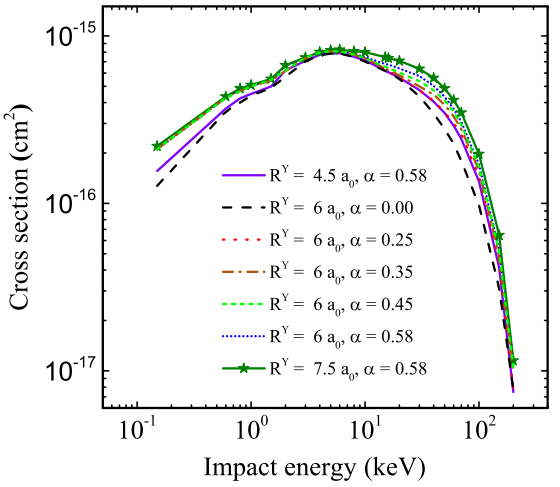

FIG. 3. Total capture cross sections calculated with various combinations of R^{Υ} and α with R^{Υ} ranging from 4.5 a_0 to 7.5 a_0 and α from 0 to 0.58. Note that collision configuration (a) is employed, see Fig. 2(a).

view of the strength of the mutual interactions: for $0.0 \leqslant b \leqslant 2.9$ a_0, it is varied in a step of $\Delta b = 0.1$ a_0, and for $2.9 < b \leqslant 11.9$ a_0, Δb becomes 0.2 a_0. With this partition, we totally calculated 75 collision events for each configuration. Similar calculations were repeated for other collision configurations in Fig. 2. Note that it is always beneficial to check the reliability and robustness of numerical parameters, e.g., box size, grid spacing, time step, and absorbing width, and we find that the present adopted parameters suffice to ensure the convergence of the present results. Furthermore, we want to emphasize that adding more initial configurations and refined impact parameters may improve the accuracy of the results [32] presented in this work, but it is not expected to drastically alter the major results in this study.

III. RESULTS AND DISCUSSIONS

A. Test calculations of convergence

As mentioned in Sec. II B, our method to extract the electron capture and ionization cross sections involves two empirical parameters, the radius of electronic density of the projectile R^{Υ} and the introduced parameter α, thus it would be good to check the results' convergence on these two parameters prior to direct comparisons of calculated results with available experimental data. To that end, we calculated the total capture cross sections using Eqs. (8), (11), and (13), for sets of (R^{Υ}, α) by varying the R^{Υ} from 4.5 a_0 to 7.5 a_0 and α from 0 to 0.58, and illustrative results, obtained from the collision configuration (a), are presented in Fig. 3.

Basically, various groups of (R^{Υ}, α) yield the total capture cross sections with similar parabolic energy profile and comparable magnitude, which nearly converges at impact energies in excess of 100 keV. For the fixed α, e.g., $\alpha = 0.58$, we find that the increase in the radius R^{Υ} results in larger cross sections, for instance, factor-of-two discrepancies can be observed both at low and at high collision energies when varying R^{Υ}, but there is no significant difference when changing $R^{\Upsilon} = 6$ a_0 to 7.5 a_0, which may indicate that a radius of 6 a_0 is large enough to ensure converged results, which is identical to that used in H^+-Be collisions in Ref. [47].

Based on $R^{\Upsilon} = 6$ a_0, we systematically varied α from 0 to 0.58 to see its influence on the cross sections. In Fig. 3, remarkable differences can be observed between $\alpha = 0$ and 0.25, where the latter provides relatively large results (enhanced by nearly a factor of 2 at low energies). However, one can see it becomes less sensitive for the values larger than 0.25. It is to be noted that much larger α, for instance, $\alpha = 0.7$, are meaningless in our analysis, since lower bound of $(t_1 - \alpha t_{2-1})$ is already earlier than the onset of sizable ionizations. Strictly speaking, the proton capture radius depends on what n-state the captured electron goes to. However, the focus of this work is not on the state-resolved analysis of the projectile, instead we approximate the capture ability of proton by an effective capture radius of a few Bohr, which may to some extent influence the results' precision, but we do not expect the change by orders of magnitude. Although R^{Υ} and α are empirically adjustable parameters, we tested many groups of (R^{Υ}, α), without taking the relevant experiments as the benchmark, to prove that the electron capture cross sections are converged approximately at $R^{\Upsilon} = 6$ a_0. In addition to this, we also applied the present approach to the case of H^++H collisions in the energy range of interest, the calculated total capture cross sections agree exceedingly well with previous experiments within the errors of less than 1%, which somewhat demonstrates the applicability of the present approach. In the following sections, we shall analyze the cross sections and associated probabilities with the parameters $R^{\Upsilon} = 6$ a_0 and $\alpha = 0.25$ for consistency.

B. Electron loss probabilities

We calculated probabilities for single-, double-, triple-, and quadruple-electron loss $2\pi P_k^{\rm loss} b$ (k = 1, 2, 3, 4). The results at three impact energies of 1, 10, and 100 keV are presented

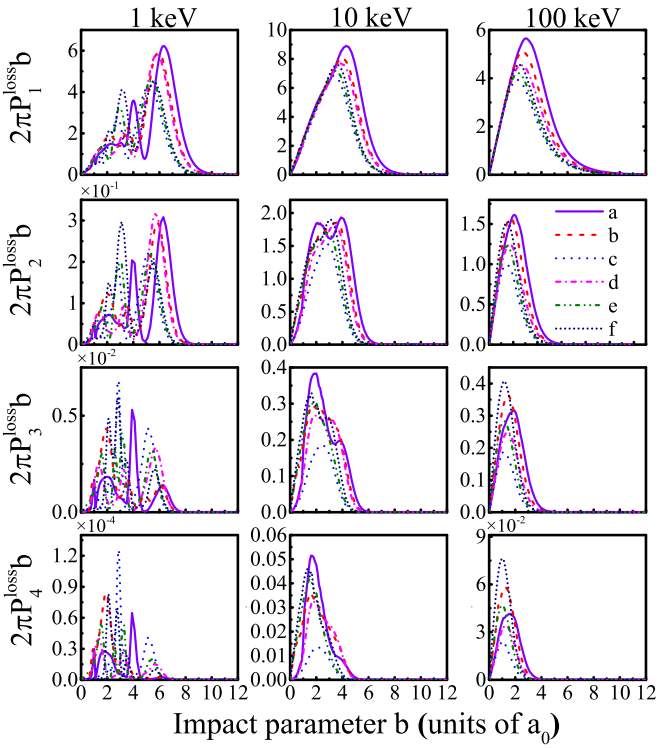

FIG. 4. Electron loss probabilities of single-, double-, triple-, and quadruple-electron loss as a function of the impact parameter, at three impact energies of 1 (left), 10 (middle), and 100 keV (right). Results for various configurations are denoted by different types of curves.

in Fig. 4 as functions of b for six collision configurations. It can be seen that electron loss probabilities decrease by orders of magnitude with increasing the electron loss number, irrespective of impact energies. Probabilities for more than five-electron loss (not shown) are negligible. For the given impact energy, probabilities tend to converge towards low impact parameters as the number of electron loss grows, for instance, at 10 keV, the converged impact parameters are 9, 7, 6, and 5 a_0 for $k = 1$, 2, 3, and 4, respectively. This fact indicates that high-order electron losses are more likely to occur in close collisions, which has already been observed in the cases of H^++Ar [57] and $H^+ + H_2O$ [29] collisions. As changing the impact energy from 1 through 10 keV to 100 keV, we find that electron loss probabilities first undergo rising and then decreasing except for the quadruple-electron loss case, which suggests that total electron loss cross sections are dominant near 10 keV. Comparing the results from various configurations, electron loss probabilities significantly depend on the N_2's alignment; in other words, pronounced orientation effects are observed.

It was found in atomic collisions both experimentally and theoretically that ionization dominates over the electron capture at high energies [6,58], typically on the order of 100 keV. To verify the described scenario in molecular collisions studied here, Fig. 5 shows orientation-averaged electron capture probabilities (solid curves) and ionization probabilities (dashed curves) for 1 keV, 10 keV, and 100 keV, respectively. By comparison, it is obvious that the mechanism of electron loss depends strongly on the impact energy: at low energies (e.g., 1 keV) electron capture process is distinctly dominant, whereas

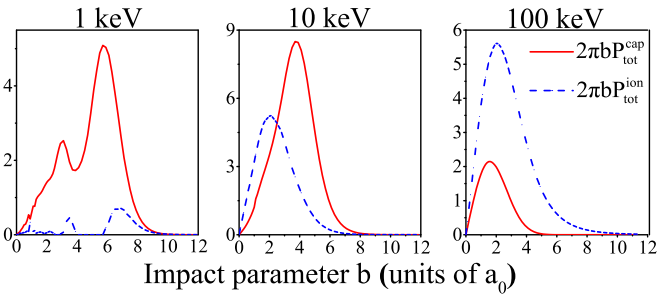

FIG. 5. Comparison between electron capture probabilities (solid curves) and ionization probabilities (dashed curves). Three impact energies of 1 (left), 10 (middle), and 100 keV (right) are illustrated.

electron ionization process becomes the leading one at high energies (e.g., 100 keV). Besides, our observation is also consistent with the major findings in $H^+ + H_2O$ [29] collisions.

C. Electron capture and ionization cross sections

Through integrating the associated probabilities over the impact parameters and then averaging over six collision configurations, the total electron capture cross sections σ_{tot}^{cap} and total ionization cross sections σ_{tot}^{ion} are calculated as shown in Figs. 6 and 7, in which experimental results [59–71] and semi-empirical calculations [72,73] are also presented for comparison where available.

In Fig. 6(c), the electron capture cross sections measured by different groups all show a maximum in the energy region 3–10 keV, beyond which the cross sections monotonically decrease when the impact energies are increased or decreased. In this respect, the calculated results are able to reproduce the experimental data in the considered energy range, but with underestimated magnitudes to a certain degree for impact energies 3–10 keV. For a quantitative comparison, the present results underestimated experimental data, especially for impact energies lower than 10 keV, for example, the calculated results are roughly 50% lower than early data by Gao *et al.* [70] and about 20% lower than those by Barnett *et al.* [60]. We find that the CTMC calculations [74] based on the model potential could qualitatively reproduce the experiments only at high-impact energies (>10 keV), and it faces formidable difficulties at low energies [74] because the simple model potential cannot describe the problem where quantum effects cannot be negligible. Since experimental data are almost consistent with each other, the discrepancy between present results and experiments may be attributed to (i) The insufficient *e-e* correlation. It is well known that the electron correlation plays a crucial role in molecular collisions at low energies [75–77], particularly below 10 keV/amu. For example, for He^{2+}+He collisions, it has been reported that adiabatic correlations support the fact that double electron capture dominates over single capture at low energies [77,78], whereas actually the experiments observed the dominance of single capture at those energies [79]. (ii) The approximate method to extract the cross sections. In our treatment, the main assumption consists in the constant electron ionization rate over the period of proton passing across the boundary, which, however, is rather critical for nonequilibrium dynamics. Since the lack of more accurate benchmark studies of H^+-N_2 collisions within TDDFT method, e.g., based

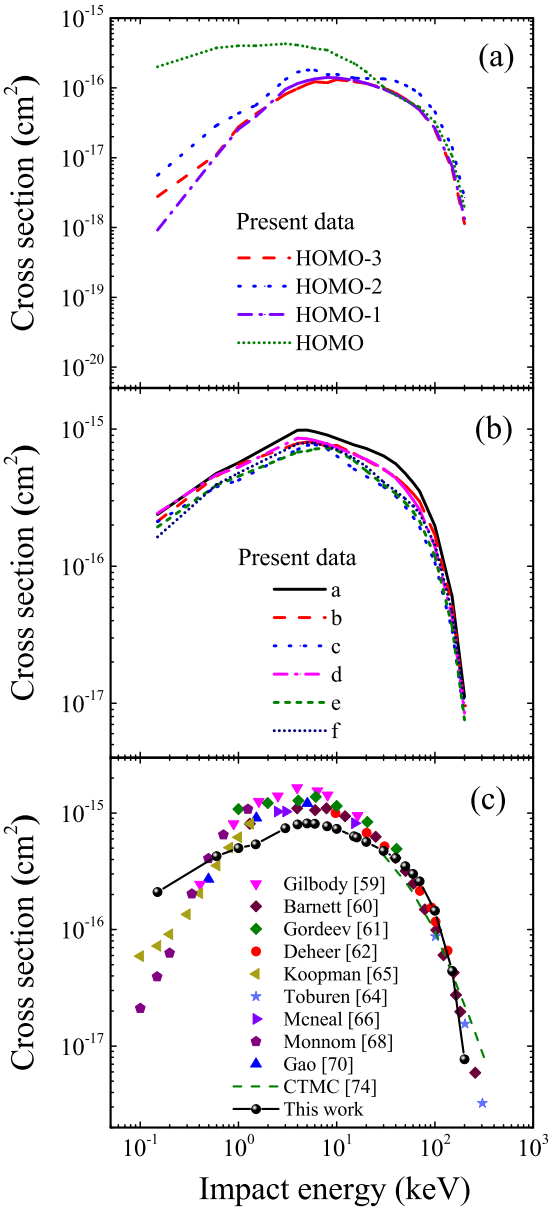

FIG. 6. Total electron capture cross sections. (a) Orbital contributions, (b) orientation contributions, (c) comparison to experimental data as a function of impact energies. Other symbols are experimental results of Gilbody *et al.* from Ref. [59], Barnett *et al.* from Ref. [60], Gordeev *et al.* from Ref. [61], Deheer *et al.* from Ref. [62], Koopman *et al.* from Ref. [65], Toburen *et al.* from Ref. [64], Mcneal *et al.* from Ref. [66], Monnom from Ref. [68], and Gao *et al.* obtained from Ref. [70]. Previous CTMC data are cited from Ref. [74]. Lines are drawn to guide the eyes for present results.

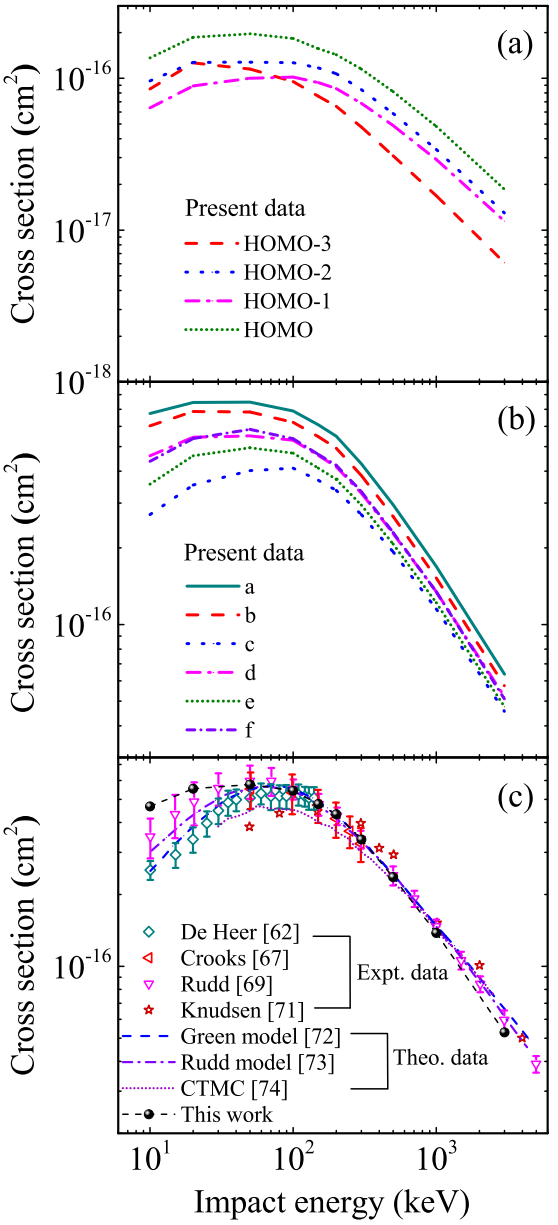

FIG. 7. Same as Fig. 6, but for total ionization cross sections. Symbols in panel (c) are experimental results of De Heer *et al.* from Ref. [62], Crooks *et al.* from Ref. [67], Rudd *et al.* from Ref. [69], Knudsen *et al.* obtained from Ref. [71]. Previous theoretical data are cited from Green *et al.* [72], Rudd *et al.* [73], and L. Errea *et al.* [74]. Lines are drawn to guide the eyes for present results.

on the OPM for the propagation and the density matrix for the extraction of measurable quantities, it is still unknown that the observed discrepancies result mainly from which factor discussed above. Taking these into account, we can preliminarily conclude that present results agree reasonably well with experimental results.

We have to emphasize that for the energies higher than 200 keV, the present method of the classical partition by considering the volume Υ fails to describe the electron capture cross sections (not shown), underestimating it by at least an order of magnitude. This main deficiency originates from the way how we extract the capture probability, because ultrahigh projectile velocities are typically characterized by sub-fs time scales resulting in the capture probabilities numerically indistinguishable from electron loss probabilities in our cases. This, however, is not a problem for a density matrix method [24]. In addition, to our knowledge, other *ab initio* theoretical calculations are absent for total electron capture cross sections of $H^+ + N_2$ collisions in this energy region. Therefore, more accurate calculations by high-level theoretical modelings [24,80,81] are necessary to be conducted.

We also analyzed multielectron effects of N_2 by calculating orbital-resolved electron capture cross sections presented in Fig. 6(a). It is found that the highest-occupied molecular orbital (HOMO) dominates over other orbitals for energies lower than 20 keV, and the inner shells contribute almost by an order of magnitude lower. At higher energies, orbital contributions are nearly convergent, although inner orbitals (HOMO-2) become important. Regarding the configuration specified capture cross sections in Fig. 6(b), they exhibit quite a similar tendency as well as magnitudes, and thus the orientation effects are not as pronounced as that seen in the electron loss probabilities. In Fig. 6(b), configuration (a) always gives relatively larger capture cross sections than all other cases, which can be explained in terms of configuration geometry in Fig. 2. In fact, the configuration (a) corresponds to the situation that the proton impinges the target perpendicular to the N-N bond, where the proton passes through denser electron cloud by the two-center scattering.

Figure 7 presents the total ionization cross sections $\sigma_{\rm tot}^{\rm ion}$, alongside the pertinent experimental data and theoretical calculations. We find that our results agree well with experimental as well as theoretical results, in particular for energies higher than 50 keV, whereas CTMC simulations [74] slightly underestimated the experiments. For those lower than 50 keV, our results are overestimated, which may be probably affected by the capture cross sections that are underestimated in the same energy range, as an indirect approach has been adopted to calculate the ionization cross sections, see Eqs. (14) and (15). Taking into account experimental uncertainties from Rudd *et al.* [69], our results seem acceptable to some extent. In this energy region, theoretical model by Green *et al.* [72] and Rudd *et al.* [73] predicted the measurements extremely well, in contrast, the present results deviate significantly from experimental points. It is noteworthy that both the Green [72] and Rudd model [73] are semi-empirical models, which have been built upon the fittings to experimentally measured proton-impact ionization cross sections of various gaseous atoms and molecules. For this reason, it is not surprising that Green and Rudd models reproduce well the experimental data. It can also be seen that $\sigma_{\rm tot}^{\rm ion}$ attains a maximum of $\sim 5 \times 10^{-16}$ cm^2 in the energy range of 50–100 keV, in which efficient electron ionizations appear. Furthermore, the observed quantitative agreement at high energies ($\geqslant$100 keV) implies that the present method is valid to predict ionization cross sections in this energy region.

As discussed in Fig. 6, we also study orbital and orientation dependence for ionization cross sections, shown in Figs. 7(a) and 7(b), respectively. It can be seen in Fig. 7(a) that the HOMO is predominant in the whole energy region considered, but inner shell ionizations are also notable and divergent, which is obviously different from that observed in Fig. 6(a). From Fig. 7(b), remarkable orientation effects of ionization cross sections can be observed, and thus electron cloud distributions can indeed significantly influence the ionization dynamics.

IV. CONCLUSION

We theoretically study the proton in collisions with the N_2 molecule in the energy range of 0.6–3000 keV, in particular we calculate electron capture and ionization cross sections. For this purpose, we work with the time-dependent density-functional theory at the level of the adiabatic local-density approximation augmented with a self-interaction correction. Classical molecular dynamics that is nonadiabatically coupled to electron dynamics is used to simulate nuclear motions. In our TDDFT-MD calculations, we propose an approximate method to extract the electron capture cross sections, which assumes constant electron ionization rate over the time period of proton passing across the boundary. On the whole, our results agree reasonably well with the experimental data and semi-empirical results in the energy region considered. For electron capture cross sections, we slightly underestimated the experiments for energies 1–10 keV, but for higher energies we predict the measured results quite well. For electron ionization cross sections, the present results seem to somewhat overestimate the experiments for energies lower than 50 keV, but still acceptable within the experimental uncertainties. Calculated high-energy ionization cross sections are in good agreement with experiments.

The present paper shows an approximate method to calculate electron capture and ionization probabilities from KSOs, which does not explicitly calculate the density matrix or overlap integrals. There remains the introduced empirical parameters, the radius of the volume accounting for electron capture and the smoothing factor for the ionization rate, which has to be carefully tested, independent of experimental data, to ensure the convergence before systematic studies. As a crude approximation, the disadvantage of the present method is also clear, it fails to tackle the electron capture taking place at energies of the order of 100 keV, and the electron ionization cross sections lower than 10 keV have not been reproduced well. Compared to the density matrix approach, our method is unable to deal with the more challenging problems in ion-atom and ion-molecule collisions, such as ionized wave-packet contributions [82], bound-state probabilities [46], the asymptotic problem of continuum electrons [83], and fragmentation cross sections [24]. After all, if one is interested in calculating total cross sections at keV energies with no advanced models at hand, the present method may be helpful. As an ambitious goal to accurately reveal the collision dynamics for $H^+ + N_2$ collisions in a broad range of energy, high-level theoretical modelings, including the correct treatment of interaction potential and direct analysis of final scattering states, are further required.

ACKNOWLEDGMENTS

The authors wish to thank the anonymous referee for constructive criticism and enlightening remarks. We thank Professor Bin He (IAPCM) and Dr. Xuhai Hong for stimulating discussions. This work was supported by the National Key Research and Development Program of China under Grant No. 2017YFA0402300, the National Magnetic Confinement Fusion Program with Grant No. 2015GB117000, and by the National Science Foundation of China under Contracts No. 11704039, No. 11404065, No. 11674067, and No. 11774030. One of the authors (C.-Z. G.) was funded, in part, by the China Postdoctoral Science Foundation (Grant No. 2017M610819).

[1] Y. S. Katharria, S. Kumar, F. Singh, J. C. Pivin, and D. Kanjilal, J. Phys. D **39**, 3969 (2006).
[2] R. Hellborg, H. J. Whitlow, and Y. W. Zhang, *Ion Beams in Nanoscience and Technology* (Springer-Verlag, Berlin, 2009).
[3] I. P. Jain and G. Agarwal, Surf. Sci. Rep. **66**, 77 (2011).
[4] J. Ullrich, R. Moshammer, A. Dorn, R. Dörner, L. P. H. Schmidt, and H. Schmidt-Böcking, Rep. Prog. Phys. **66**, 1463 (2003).
[5] W. Fritsch and C. D. Lin, Phys. Rep. **202**, 1 (1991).
[6] B. H. Bransden and M. R. C. McDowell, *Charge Exchange and the Theory of Ion-Atom Collisions* (Clarendon, New York, 1992).
[7] M. E. Rudd, Y.-K. Kim, D. H. Madison, and T. J. Gay, Rev. Mod. Phys. **64**, 441 (1992).
[8] R. Abrines and I. C. Percival, Proc. Phys. Soc. **88**, 861 (1966).
[9] R. E. Olson and A. Salop, Phys. Rev. A **16**, 531 (1977).
[10] H. Ryufuku, K. Sasaki, and T. Watanabe, Phys. Rev. A **21**, 745 (1980).
[11] A. Niehaus, J. Phys. B: At. Mol. Opt. Phys. **19**, 2925 (1986).
[12] L. Liu, C. H. Liu, J. G. Wang, and R. K. Janev, Phys. Rev. A **84**, 032710 (2011).
[13] R. T. Zhang *et al.*, Phys. Rev. A **95**, 042702 (2017).
[14] E. Runge and E. K. U. Gross, Phys. Rev. Lett. **52**, 997 (1984).
[15] C. Ullrich, *Time-Dependent Density-Functional Theory: Concepts and Applications* (Oxford University Press, New York, 2012).
[16] S. Kümmel and L. Kronik, Rev. Mod. Phys. **80**, 3 (2008).
[17] B. Zygelman and A. Dalgarno, Phys. Rev. A **33**, 3853 (1986).
[18] L. L. Yan, L. Liu, Y. Wu, Y. Z. Qu, J. G. Wang, and R. J. Buenker, Phys. Rev. A **88**, 012709 (2013).
[19] F. Calvayrac, P.-G. Reinhard, E. Suraud, and C. A. Ullrich, Phys. Rep. **337**, 493 (2000).
[20] R. O. Jones, Rev. Mod. Phys. **87**, 897 (2015).
[21] N. T. Maitra, J. Chem. Phys. **144**, 220901 (2016).
[22] H. J. Ludde and R. M. Dreizler, J. Phys. B: At. Mol. Opt. Phys. **16**, 3973 (1983).
[23] H. J. Lüdde, T. Spranger, M. Horbatsch, and T. Kirchner, Phys. Rev. A **80**, 060702 (2009).
[24] M. Murakami, T. Kirchner, M. Horbatsch, and H. J. Lüdde, Phys. Rev. A **85**, 052704 (2012).
[25] A. Salehzadeh and T. Kirchner, Eur. Phys. J. D **71**, 66 (2017).
[26] M. Murakami, T. Kirchner, M. Horbatsch, and H. J. Lüdde, Phys. Rev. A **86**, 022719 (2012).
[27] A. C. K. Leung and T. Kirchner, Phys. Rev. A **95**, 042703 (2017).
[28] F. Wang, X. Hong, J. Wang, and K. S. Kim, J. Chem. Phys. **134**, 154308 (2011).
[29] X. Hong, F. Wang, Y. Wu, B. Gou, and J. Wang, Phys. Rev. A **93**, 062706 (2016).
[30] J. P. Perdew and A. Zunger, Phys. Rev. B **23**, 5048 (1981).
[31] C. Legrand, E. Suraud, and P. Reinhard, J. Phys. B: At. Mol. Opt. Phys. **35**, 1115 (2002).
[32] C.-Z. Gao, J. Wang, F. Wang, and F.-S. Zhang, J. Chem. Phys. **140**, 054308 (2014).
[33] E. E. Quashie, B. C. Saha, X. Andrade, and A. A. Correa, Phys. Rev. A **95**, 042517 (2017).
[34] L. Gulyás, T. Kirchner, T. Shirai, and M. Horbatsch, Phys. Rev. A **62**, 022702 (2000).
[35] R. Nagano, K. Yabana, T. Tazawa, and Y. Abe, Phys. Rev. A **62**, 062721 (2000).
[36] P. Ehrenfest, Z. Phys. **45**, 455 (1927).
[37] S. Goedecker, M. Teter, and J. Hutter, Phys. Rev. B **54**, 1703 (1996).
[38] A. Castro, M. Isla, J. I. Martínez, and J. A. Alonso, Chem. Phys. **399**, 130 (2012).
[39] S. Bubin, B. Wang, S. Pantelides, and K. Varga, Phys. Rev. B **85**, 235435 (2012).
[40] F. Mao, C. Zhang, C.-Z. Gao, J. Dai, and F.-S. Zhang, J. Phys. Condens. Matter **26**, 085402 (2014).
[41] M. Horbatsch, J Phys. B: At. Mol. Opt. Phys. **22**, L639 (1989).
[42] M. Zapukhlyak, T. Kirchner, A. Hasan, B. Tooke, and M. Schulz, Phys. Rev. A **77**, 012720 (2008).
[43] C. Ullrich, J. Mol. Struct.: THEOCHEM **501**, 315 (2000).
[44] J. M. Rost, Phys. Rev. Lett. **82**, 1652 (1999).
[45] A. G. Borisov and J. P. Gauyacq, Phys. Rev. B **62**, 4265 (2000).
[46] A. Kołakowska, M. S. Pindzola, and D. R. Schultz, Phys. Rev. A **59**, 3588 (1999).
[47] S. Zhao, W. Kang, J. Xue, X. Zhang, and P. Zhang, Phys. Lett. A **379**, 319 (2015).
[48] F. Mao, C. Zhang, J. Dai, and F.-S. Zhang, Phys. Rev. A **89**, 022707 (2014).
[49] P. M. Dinh, P.-G. Reinhard, E. Suraud, and P. Wopperer, Eur. Phys. J. D **69**, 61 (2015).
[50] R. M. Dreizler and E. K. U. Gross, *Density Functional Theory* (Springer-Verlag, Berlin, 1990).
[51] P.-G. Reinhard and R. Cusson, Nucl. Phys. A **378**, 418 (1982).
[52] K.-P. Huber, *Molecular Spectra and Molecular Structure: IV. Constants of Diatomic Molecules* (Springer, New York, 2013).
[53] J.-H. Fock, P. Gürtler, and E.-E. Koch, Chem. Phys. **47**, 87 (1980).
[54] W. Yu, Y. Zhang, F. S. Zhang, R. Hutton, Y. Zou, C.-Z. Gao, and B. Wei, J. Phys. B: At. Mol. Opt. Phys. **51**, 035204 (2018).
[55] M. Feit, J. Fleck, and A. Steiger, J. Comput. Phys. **47**, 412 (1982).
[56] L. Verlet, Phys. Rev. **159**, 98 (1967).
[57] F. Wang, X. Xu, X. Hong, J. Wang, and B. Gou, Phys. Lett. A **375**, 3290 (2011).
[58] L. Liu, X. Li, J. Wang, and R. Janev, Phys. Plasmas **21**, 062513 (2014).
[59] H. Gilbody and J. Hasted, in *Proceedings of the Royal Society of London A: Mathematical, Physical and Engineering Sciences* (The Royal Society, London, 1957), Vol. 238, pp. 334–343.
[60] C. F. Barnett and H. K. Reynolds, Phys. Rev. **109**, 355 (1958).
[61] Y. S. Gordeev and M. N. Panov, Sov. Phys. Tech. Phys. **9**, 656 (1964).
[62] F. De Heer, J. Schutten, and H. Moustafa, Physica **32**, 1766 (1966).
[63] L. M. Welsh, K. H. Berkner, S. N. Kaplan, and R. V. Pyle, Phys. Rev. **158**, 85 (1967).
[64] L. H. Toburen, M. Y. Nakai, and R. A. Langley, Phys. Rev. **171**, 114 (1968).
[65] D. W. Koopman, Phys. Rev. **166**, 57 (1968).
[66] R. J. McNeal and D. C. Clark, J. Geophys. Res. **74**, 5065 (1969).
[67] J. B. Crooks and M. E. Rudd, Phys. Rev. A **3**, 1628 (1971).
[68] G. Monnom, M. Eliot, J. Guidini, and F. P. G. Valckx, C. R. Acad. Sci. Paris **281**, 425 (1975).
[69] M. E. Rudd, R. D. DuBois, L. H. Toburen, C. A. Ratcliffe, and T. V. Goffe, Phys. Rev. A **28**, 3244 (1983).
[70] R. S. Gao, L. K. Johnson, C. L. Hakes, K. A. Smith, and R. F. Stebbings, Phys. Rev. A **41**, 5929 (1990).
[71] H. Knudsen, U. Mikkelsen, K. Paludan, K. Kirsebom, S. P. Moller, E. Uggerhoj, J. Slevin, M. Charlton, and E. Morenzoni, J. Phys. B: At. Mol. Opt. Phys. **28**, 3569 (1995).

[72] A. E. S. Green and R. J. McNeal, J. Geophys. Res. **76**, 133 (1971).
[73] M. E. Rudd, Y. K. Kim, D. H. Madison, and J. W. Gallagher, Rev. Mod. Phys. **57**, 965 (1985).
[74] L. Errea, C. Illescas, L. Méndez, and I. Rabadán, Appl. Radiat. Isot. **83**, 86 (2014).
[75] D. Belkić, I. Mančev, and J. Hanssen, Rev. Mod. Phys. **80**, 249 (2008).
[76] D. Belkić, J. Math. Chem. **47**, 1366 (2010).
[77] M. Baxter and T. Kirchner, Phys. Rev. A **93**, 012502 (2016).
[78] K. J. Schaudt, N. H. Kwong, and J. D. Garcia, Phys. Rev. A **43**, 2294 (1991).
[79] R. D. DuBois, Phys. Rev. A **36**, 2585 (1987).
[80] S. Mada, K.-N. Hida, M. Kimura, L. Pichl, H.-P. Liebermann, Y. Li, and R. J. Buenker, Phys. Rev. A **75**, 022706 (2007).
[81] P. M. M. Gabás, L. F. Errea, L. Méndez, and I. Rabadán, Phys. Rev. A **85**, 012702 (2012).
[82] M. Chassid and M. Horbatsch, Phys. Rev. A **66**, 012714 (2002).
[83] T.-G. Lee, S. Y. Ovchinnikov, J. Sternberg, V. Chupryna, D. R. Schultz, and J. H. Macek, Phys. Rev. A **76**, 050701 (2007).